

# Electrical monitoring of single-event protonation dynamics at the solid-liquid interface and its regulation by external mechanical forces

Received: 21 February 2024

Accepted: 4 October 2024

Published online: 13 October 2024

 Check for updates

Cong Zhao<sup>1,6</sup>, Jiazheng Diao<sup>2,6</sup>, Zhao Liu<sup>1,6</sup>, Jie Hao<sup>1</sup>, Suhang He<sup>1</sup>, Shaojia Li<sup>1</sup>, Xingxing Li<sup>2,3</sup>, Guangwu Li<sup>1,4</sup> , Qiang Fu<sup>2,3</sup> , Chuancheng Jia<sup>1</sup>  & Xuefeng Guo<sup>1,5</sup> 

Detecting chemical reaction dynamics at solid-liquid interfaces is important for understanding heterogeneous reactions. However, there is a lack of exploration of interface reaction dynamics from the single-molecule perspective, which can reveal the intrinsic reaction mechanism underlying ensemble experiments. Here, single-event protonation reaction dynamics at a solid-liquid interface are studied in-situ using single-molecule junctions. Molecules with amino terminal groups are used to construct single-molecule junctions. An interfacial cationic state present after protonation is discovered. Real-time electrical measurements are used to monitor the reversible reaction between protonated and deprotonated states, thereby revealing the interfacial reaction mechanism through dynamic analysis. The protonation reaction rate constant has a linear positive correlation with proton concentration, whereas the deprotonation reaction rate constant has a linear negative correlation. In addition, external mechanical forces can effectively regulate the protonation reaction process. This work provides a single-molecule perspective for exploring interface science, which will contribute to the development of heterogeneous catalysis and electrochemistry.

Investigating chemical reaction dynamics is of significance for revealing their intrinsic mechanisms, especially those at solid-liquid interfaces. Such reactions are requisite to heterogeneous catalysis<sup>1-3</sup> and electrochemistry<sup>4-6</sup>, and are closely related to material synthesis<sup>7,8</sup> and energy storage<sup>9</sup>. Over the past decades, several macroscopic techniques have been developed to study the reaction processes at solid-

liquid interfaces, such as in-situ Raman spectroscopy<sup>10</sup> and surface-enhanced infrared absorption spectroscopy<sup>11</sup>. However, in macroscopic experiments, the details of the individual reaction steps that comprise the entire reaction pathway are obscured by the quasi-equilibrium conditions of the ensemble. Direct detection of reactions at solid-liquid interfaces and analysis of reaction dynamics at the

<sup>1</sup>Center of Single-Molecule Sciences, Institute of Modern Optics, Frontiers Science Center for New Organic Matter, Tianjin Key Laboratory of Micro-Scale Optical Information Science and Technology, College of Electronic Information and Optical Engineering, Nankai University, Tianjin, China. <sup>2</sup>Hefei National Research Center for Physical Sciences at the Microscale, School of Future Technology, University of Science and Technology of China, Hefei, China. <sup>3</sup>Hefei National Laboratory, University of Science and Technology of China, Hefei, China. <sup>4</sup>Shenzhen Research, Institute of Nankai University, 16th Floor, Yantian Science & Technology Building, Shenzhen, China. <sup>5</sup>Beijing National Laboratory for Molecular Sciences, National Biomedical Imaging Center, College of Chemistry and Molecular Engineering, Peking University, Beijing, China. <sup>6</sup>These authors contributed equally: Cong Zhao, Jiazheng Diao, Zhao Liu.

 e-mail: [ligw@nankai.edu.cn](mailto:ligw@nankai.edu.cn); [qfu3@ustc.edu.cn](mailto:qfu3@ustc.edu.cn); [jiacc@nankai.edu.cn](mailto:jiacc@nankai.edu.cn); [guoxf@pku.edu.cn](mailto:guoxf@pku.edu.cn)

single-event or -molecule level provide opportunities to deepen our understanding of reaction mechanisms. Therefore, a reliable in-situ technique to monitor single-molecule reaction dynamics at solid-liquid interfaces is required.

Single-molecule junctions (SMJs)<sup>12–15</sup> can be used to in-situ monitor chemical reaction processes in solution at the single-event level<sup>16–20</sup>. In SMJs, single molecules with specific terminal groups can behave as molecular bridges between two electrodes and be monitored by real-time electrical signals. For example, graphene-based SMJs are an effective platform for studying single-molecule chemical reactions and analyzing reaction dynamics<sup>21–24</sup>. In this approach, a single molecule bridges between two electrodes through robust covalent amide bonds<sup>25</sup>, which allows efficient monitoring of the chemical reaction on the functional center of the molecule. When it comes to ions involved in metal-solution interfacial reactions, single-molecule break junctions based on metal electrodes are more appropriate. The electrical measurement of single-molecule break junctions is based on repeatedly forming and breaking molecule-electrode contacts<sup>26</sup>, and thus it is suitable for the study of metal-solution interfaces<sup>27–33</sup>. Based on this technique, it is possible to not only detect chemical reactions at metal-solution interfaces but also monitor reaction dynamics.

Proton behavior<sup>11,34</sup> at solid-liquid interfaces is central to many interfacial reactions, such as the hydrogen evolution reaction<sup>1,35</sup>. Here, we study the single-event protonation reaction dynamics at a metal-solution interface using the scanning tunneling microscopy break junction (STM-BJ) technique. Specifically, the protonation reaction of an amino group, as a typical system for exploring the solid-liquid interfacial reaction, is investigated (Fig. 1a). Single molecules with amino terminal groups are used as molecular probes to detect the protonation reaction at the solid-liquid interface from the single-event perspective (Fig. 1b). By fixing the molecule to the interface, the protonation reaction dynamics can be monitored by real-time electrical measurements, allowing the overall mechanism to be interpreted. Meanwhile, the effects of proton concentration and external mechanical force on the reversible protonation reaction are explored.

## Results and Discussion

### Interfacial protonation reaction in molecular junctions

To study the single-event protonation reaction at a solid-liquid interface, gold (Au) electrodes (tip and substrate) and molecules with amino terminal groups were used to construct SMJs. Specifically, 4,4'-diamino-*p*-terphenyl (TP-N) and 4'-amino-4-thiol-*p*-terphenyl (TP-S) were chosen as the target molecules (Fig. 1b). The synthesis route of TP-S is shown in Supplementary Fig. 1. Propylene carbonate (PC) was used as a kind of polar solvent. The concentration of target molecules in PC was 1.7 mM. Trifluoromethanesulfonic acid (TFMS) and trifluoroacetic acid (TFA) were used as proton sources. Then, the STM-BJ technique allows the determination of the different protonation states through the differences in conductance during the protonation reaction.

One-dimensional (1D) and two-dimensional (2D) single-molecule conductance-displacement histograms for TP-N molecules without and with acid are presented in Fig. 2a–c and d–f, respectively. Here, the conductance peak at  $10^0 G_0$  corresponds to Au–Au point contact, where the unit  $G_0$  is the conductance quantum,  $G_0 = 2e^2/h \approx 77.5 \mu\text{S}$ <sup>36</sup>. The conductance peaks below  $10^0 G_0$  correspond to molecular signals<sup>37</sup>. Without acid, TP-N SMJs show only one conductance peak around  $\approx 10^{-3.6} G_0$  ( $\approx 19$  nS), where the amino terminal group forms a dative bond with Au at the molecule-electrode contact<sup>38,39</sup>. After the addition of TFMS (5.0 mM in PC), the junctions show a low conductance state at  $\approx 10^{-5.0} G_0$  ( $\approx 0.78$  nS; State 2). Addition of TFA also leads to the appearance of a similar low conductance state (Supplementary Fig. 2). This result is different from that in previous work, where no conductance peak appears after acid addition<sup>40</sup>. The reason

for this discrepancy is that the low conductance peak only appears in a narrow range of acid concentrations. When the acid concentration reaches  $\approx 6.67$  mM, no conductance peak is observed (Supplementary Fig. 3). The conductance of the high state (State 1) after adding  $\approx 6.67$  mM of acid is the same as that of the initial state, indicating that the molecule-electrode contact still involves a dative bond. For State 2, the conductance is much lower ( $\times 0.04$ ) than that of State 1, suggesting that the proton affects the dative bond between Au and N.

To figure out whether one or both two amino terminal groups are protonated by the acid, TP-S with one amino terminal group was further investigated. Before the electrical measurements, TP-S molecules were pre-assembled on the Au substrate for 12 h to ensure that the thiol terminal groups formed molecule-electrode contacts with stable covalent bonds, and the amino terminal groups were exposed to the solution. A conductance peak resembling that observed for TP-N after adding acid was observed when acid was added to the TP-S molecule junctions (Supplementary Fig. 4). The charge transport characteristics of the 4,4'-biphenyldithiol (BP-S), with two thiol groups and no amino group, before and after acid addition were also detected (Supplementary Figs. 5, 9). No change in conductance was observed when the same concentration of acid was added to the BP-S system, which means that acid addition could not affect the thiol terminal group. Therefore, the conductance decrease is ascribed to the protonation of the amino group. As shown in Supplementary Fig. 4d, the conductance of State 2 in the TP-S junction after acid addition is also much lower ( $\times 0.04$ ) compared with that of State 1, indicating that although there are two amino groups in a TP-N molecule, only one group is involved in the protonation reaction in State 2. On the basis of the above discussion, it can be inferred that the state with two protonated amino groups is not detected because the low conductance of such a state ( $\approx 10^{-6.5} G_0 \approx 0.025$  nS) is below the detection limit of the instrument.

To clearly understand the specific interfacial structures of State 1 and State 2, further theoretical calculations were conducted (Fig. 2g). For State 1, the N atom in the amino group is directly bonded to an Au atom, with an Au–N bond length of 2.34 Å, corresponding to the state before protonation. For State 2, a proton is located between the amino group and Au atom with corresponding N–H and Au–H bond lengths of 1.13 and 1.98 Å, respectively, which corresponds to the state after acid addition. The angles in the structures of State 1 and State 2 are listed in the Supplementary Table 1. The stability of the two configurations is confirmed by vibrational frequency analysis, which shows that they are both local minima with no imaginary frequencies. Electron localization function (ELF) analysis<sup>41</sup> (Fig. 2g) of the two configurations indicates the presence of localized electron pairs in the regions between the corresponding Au and N, N and H, as well as H and Au atoms (albeit the electron pair localization between H and Au is relatively weak), indicating the formation of chemical bonds between the atoms involved. Figure 2h presents the calculated transmission spectra for the two structures using the simulation model shown in Supplementary Fig. 7. The transmission of the configuration with directly connected amino and Au atoms is considerably higher than that of the configuration with the proton located between the N and Au atoms, which is consistent with the experimentally observed decrease in conductance after acid addition. The above results strongly indicate that both unprotonated and protonated amino terminal groups have been captured by the electrical measurements of STM-BJ.

Although the protonated amino group is isoelectronic with the methyl group, the contact between the methyl group and gold is significantly weaker than that between the protonated amino group and gold, as evidenced by the lack of a distinct conductance plateau in the conductance measurements of single 1,3,5-trimethyl-benzene (TMB) molecular junctions (Supplementary Fig. 6). Unlike the H atom in the methyl group, which is already saturated in its bonding with the C atom and therefore has no orbital interaction with the top Au atom, the proton in the protonated amino group has empty orbitals to

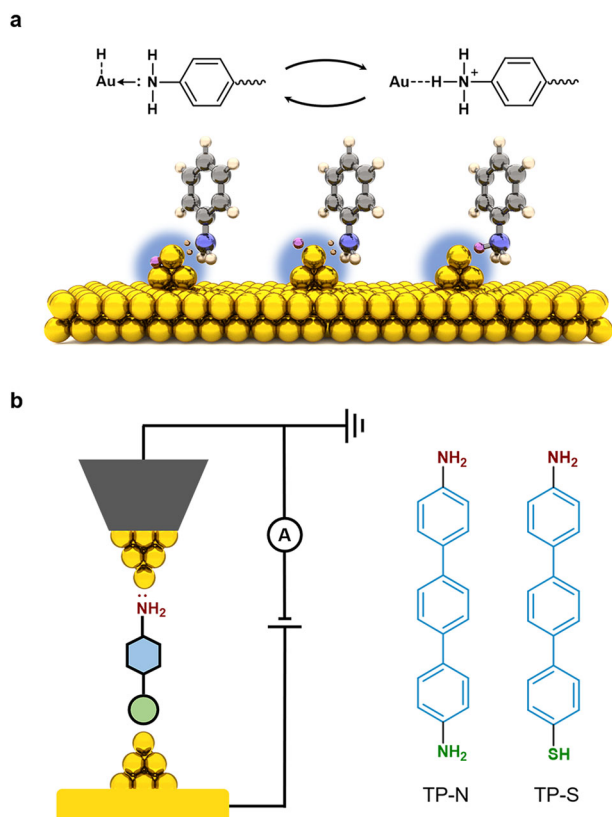


**Fig. 1 | Overview of single-event protonation reaction at the metal-solution interface.** **a** Schematic diagram for the interfacial protonation reaction of the amino group. Au, C, and N atoms are depicted in yellow, gray, and blue, respectively and H atoms are depicted in white and purple. **b** Schematic diagram for the single-molecule junction and the molecular structures.

accommodate electrons not only from the N atom (forming a coordination bond) but also from the Au. Therefore, the latter interaction is stronger than the former. The above comparison is further supported by the analysis of the ELF. It can be seen that the electron pair localization between Au and the H atom in the methyl group (Supplementary Fig. 6c) is lower than that between Au and the proton in the protonated amino group (Fig. 2g). In addition, electrostatic interactions also contribute to the binding between gold and the protonated amino group, which is augmented by the image-charge effect<sup>13</sup>.

### Dynamic analysis of the single-event protonation reaction

The typical conductance-displacement traces after adding acid reveal that the molecules spontaneously transition between State 1 and State 2 (Fig. 2f inset). By hovering the tip, conductance-time ( $G$ - $t$ ) traces can be obtained (see Supplementary Note 4, Supplementary Fig. 10). The  $G$ - $t$  histogram of pure single TP-N molecular junctions is shown in Supplementary Fig. 11, which has only one conductance state. This result also suggests the exclusion of tip retraction and molecular geometry changes in the hover mode. Then, based on a segmental  $k$ -means method of the hidden Markov model<sup>42,43</sup>, QuB software was used to collect and idealize the  $G$ - $t$  traces with two states. After idealization, dwell times of State 1 and State 2 ( $T_{S1}$  and  $T_{S2}$ ) can be obtained (Fig. 3a). The average lifetime of each state ( $\tau_{S1}$  and  $\tau_{S2}$ ) can be further derived from the probability distribution analysis of  $T_{S1}$  and  $T_{S2}$ . Taking the case with 0.83 mM TFMS as an example, both  $T_{S1}$  and  $T_{S2}$  are well fit by a single exponential decay function (Fig. 3d,e). The average lifetimes calculated through fitting are  $\tau_{S1} = 32.7 \pm 6.4$  ms and  $\tau_{S2} = 8.3 \pm 1.2$  ms. These values indicate that the protonation reaction follows a simple Poisson process. Furthermore, rate constants ( $k$ ) can

be derived from the equation  $k = 1/\tau$ . The activation energies of the protonation reaction ( $E_1$ ) and deprotonation reaction ( $E_2$ ) can be calculated from the Eyring equation  $E = RT \ln(k_B T / (hk))$ , where  $R = 8.314 \text{ J mol}^{-1} \text{ K}^{-1}$ ,  $T$  is the temperature,  $k_B$  is the Boltzmann constant, and  $h$  is the Planck constant. The energy profiles obtained from electrical experiments and theoretical simulations (with the structures in Supplementary Fig. 8) are shown in Fig. 3f. The energy barrier of the protonation reaction (from State 1 to the transition state) is  $15.4 \text{ kcal mol}^{-1}$  (calculated value of  $27.4 \text{ kcal mol}^{-1}$ ), and the energy difference between the two conductance states is  $0.8 \text{ kcal mol}^{-1}$  (calculated value of  $2.1 \text{ kcal mol}^{-1}$ ). The tunneling effect of hydrogen, which allows protons to overcome energy barriers even without sufficient energy, was not included in our simulations. As a result, the height of the effective barrier experienced by protons should be lower than the calculated energy barrier from a classical point of view, which has been demonstrated in similar calculations<sup>44-46</sup>. In addition, an implicit model is used to describe the solvent environment, which cannot account for the microscopic structural features of the solvent molecules in the vicinity of the SMJ. The structural adjustment of the solvent molecules might facilitate proton transfer between the two states, leading to an additional decrease in the energy barrier. Thus, the calculated energy barrier is higher than that obtained from the experiments. Overall, the energy profiles obtained from simulations agree well with the experimental results, indicating that the dynamic analysis of the electrical results measured by STM-BJ is reasonable. Therefore, dynamic processes of interfacial protonation reactions at the single-event level can be detected through STM-BJ measurements.

### Effect of proton concentrations on reaction dynamics

To further investigate the mechanism of this interfacial protonation reaction at the single-event level, different concentrations of TFMS were added to the TP-N system. The acid concentration is gradually increased from 0.83 to 4.17 mM, and the TP-N concentration is kept constant at 1.7 mM. The  $G$ - $t$  traces and corresponding histograms in Fig. 4a reveal that the proportion of State 2 gradually increases with increasing acid concentration, whereas the proportion of State 1 decreases. Specifically, with the increase of TFMS concentration from 0.83 to 4.17 mM, the area ratio of the peaks from State 2 (purple peaks in Fig. 4a) and State 1 (blue peaks in Fig. 4a) ( $A_{S2}/A_{S1}$ ) gradually rise from 0.20 to 8.2 (Fig. 5b, blue line). The original peak areas are shown in Supplementary Tables 3 and 4. The  $A_{S2}/A_{S1}$  values show the same trend as the macroscopic results measured by fluorescence emission spectroscopy (Supplementary Figs. 12 and 13). In emission spectra, the peak at 402 nm corresponds to neutral TP-N molecules, whereas that at 453 nm originated from TP-N molecules with one protonated amino terminal group. The spectra of fluorescence emission intensity versus acid concentration at excitation wavelengths of 402 and 495 nm indicate that the protonation reaction starts at a TFMS concentration of 0.98 mM. This concentration threshold for protonation is similar to that of the single-molecule experiments (0.83 mM, as discussed above), proving the reliability of single-molecule analysis.

Through dynamic analysis, the average lifetimes of the two states at different acid concentrations can be obtained. As shown in Fig. 4b and Supplementary Fig. 14, when the acid concentration increases from 0.83 to 4.17 mM,  $\tau_{S1}$  decreases from 32.7 to 6.1 ms, whereas  $\tau_{S2}$  increases from 8.3 to 57.3 ms. This tendency is consistent with the change in the proportion of State 1 and State 2 (Supplementary Fig. 15a). For further analysis, the rate constants for forward ( $k_f$ ) and backward ( $k_b$ ) reactions are calculated from the obtained average lifetimes of State 1 and State 2 (Fig. 4c). The ratios of rate constants ( $k_b/k_f$ ) are also shown in Supplementary Table 2, which are consistent with those obtained from macroscopic experiments. Both reaction rates exhibit a linear relationship with acid concentration. However, the correlation between  $k$  and acid concentration is different in the two

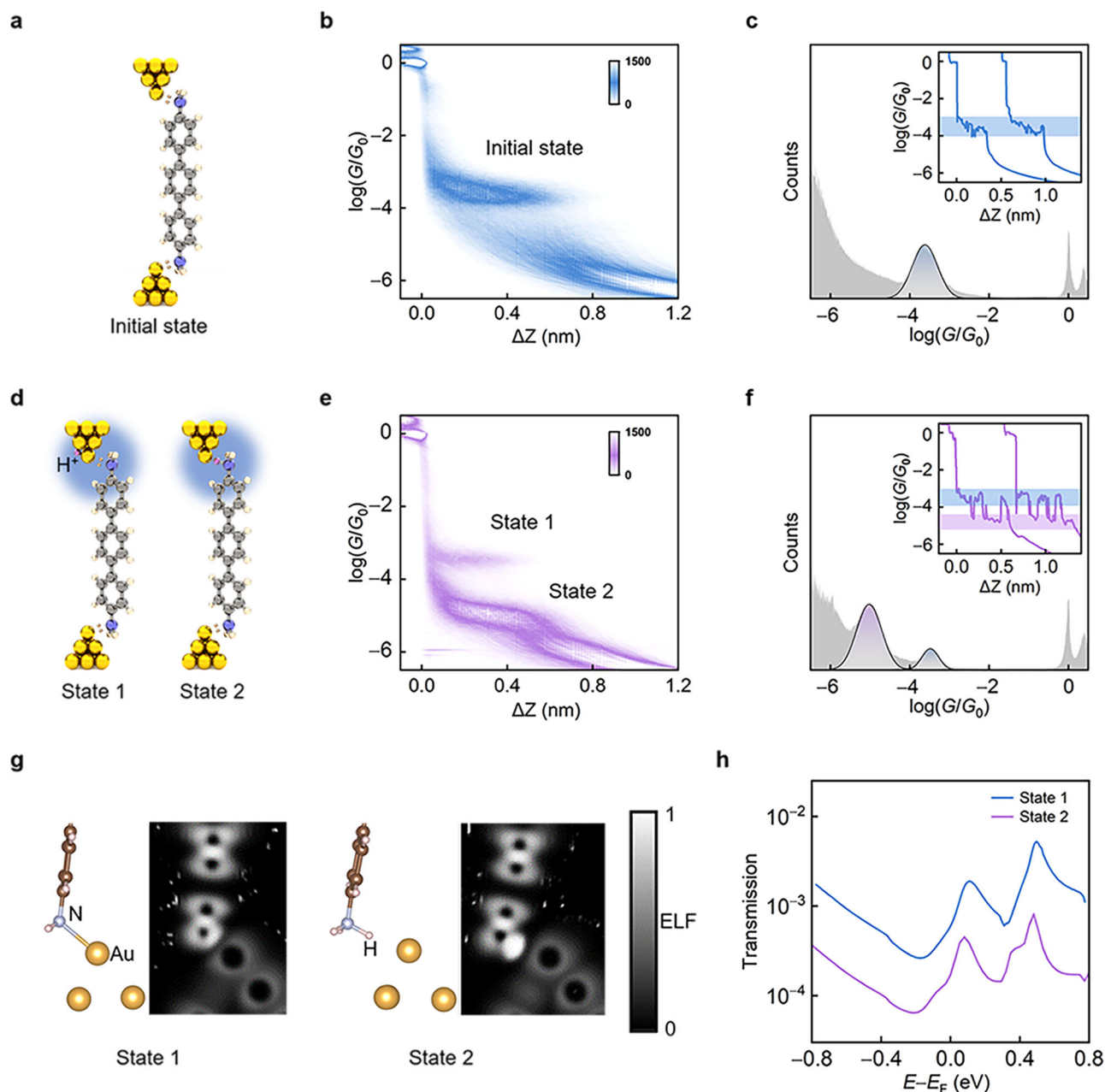


**Fig. 2 | Charge transport of single TP-N molecular junctions before and after single-event protonation reaction at the interface.** **a** Schematic diagram for single TP-N molecular junction. Au, C, and N atoms are depicted in yellow, gray, and blue, respectively and H atoms are depicted in white. **b** 2D conductance-displacement histogram for single TP-N molecular junctions, consisting of  $\approx 5700$  individual traces. The color scale shows the counts. **c** 1D conductance histogram for single TP-N molecular junctions. Inset: typical conductance-displacement traces for the junction. **d** Schematic diagram for single TP-N molecular junction with acid

addition. Au, C, and N atoms are depicted in yellow, gray, and blue, respectively and H atoms are depicted in white and purple. **e** 2D conductance-displacement histogram for the junctions with acid addition, consisting of  $\approx 6100$  individual traces. The color scale shows the counts. **f** 1D conductance histogram for junctions with acid addition. Blue: State 1; Purple: State 2. Inset: typical conductance-displacement traces for the junction. **g** Optimized configurations and calculated electron localization functions for State 1 and State 2. **h** Calculated transmission spectra for State 1 (blue) and State 2 (purple). Source data are provided as a Source Data file.

states:  $k_f$  is positively correlated with acid concentration, while  $k_b$  is negatively correlated with acid concentration. Specifically, as the acid concentration increases,  $k_f$  increases from 30.6 to 165.3  $s^{-1}$ , while  $k_b$  decreases from 120.6 to 17.5  $s^{-1}$ . This behavior is closely related to the microenvironment at the metal-solution interface. The protonation process responsible for the conductance change corresponds to proton migration between the electrode surface and anchor group of TP-N in the molecular junction. The likelihood of protonation involving proton migration from solution is very low, according to our simulations (see Supplementary Fig. 16 and Supplementary Note 7). As the acid concentration increases, protons gradually accumulate at the

solid-liquid interface. Therefore, the probability of collision between protons and amino groups at the interface increases at high acid concentrations. Consequently, the likelihood of a proton reacting with the amino group in the molecular junction is heightened, culminating in an elevated rate constant for the protonation reaction (Fig. 4d). On the contrary, the aggregation of protons leads to a higher local charge density near the amino group at the metal-liquid interface. This solvent effect impedes the proton's dissociation from the Au-H-N configuration in State 2, diminishing the likelihood of the molecule changing from State 2 to State 1 and reducing the rate constant for the deprotonation reaction.

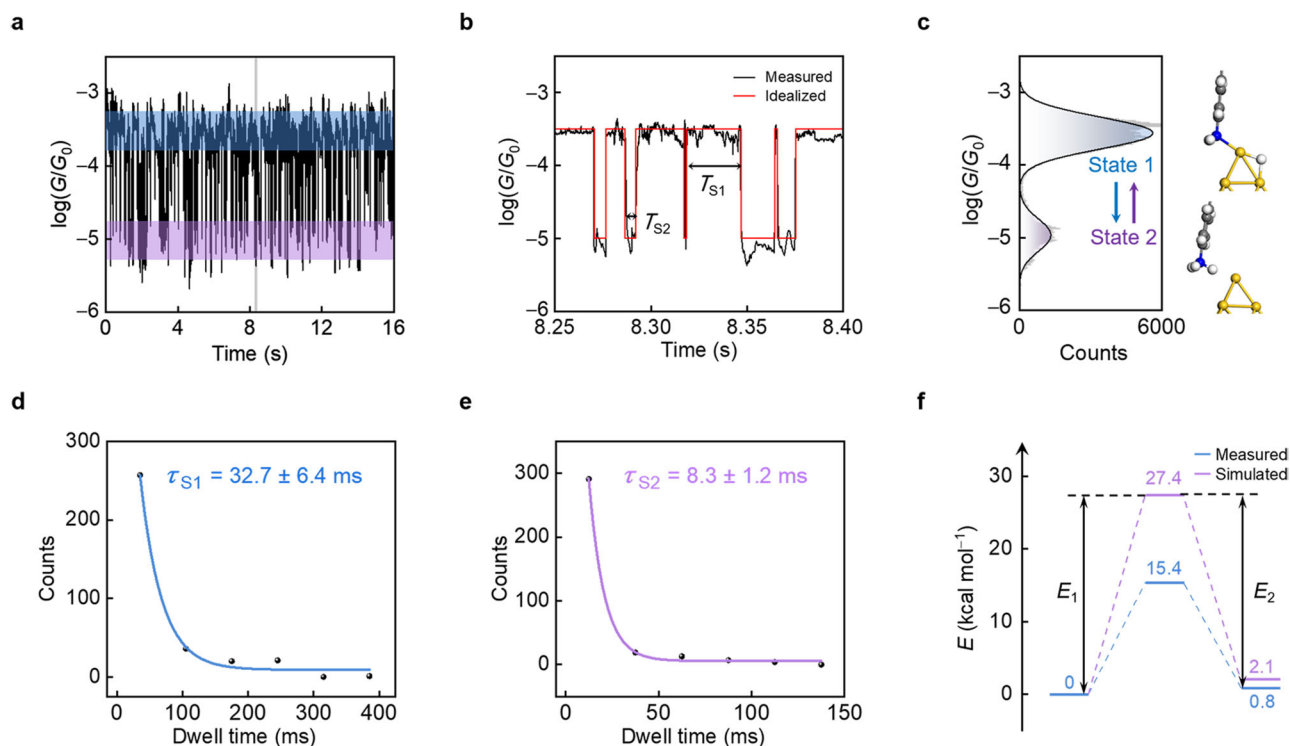


**Fig. 3 | Real-time conductance recordings and dynamic analysis.** **a** Typical  $G$ - $t$  trace of protonation reaction measured in a mixed TP-N/TFMS solution. **b** Enlarged  $G$ - $t$  trace (black) of the reaction with idealized fitting (red). **c** Corresponding histogram of conductance values, showing a bimodal conductance distribution. Au, C, N, and H atoms are depicted in yellow, gray, blue, and white, respectively. **d, e** Plots

of time intervals of State 1 (**d**) and State 2 (**e**) in the idealized fit in **a**. Single-exponential fittings derive the corresponding lifetimes. **f** Experimental (blue) and simulated (purple) energy profile of the interfacial protonation reaction. Source data are provided as a Source Data file.

### Force modulation of the interfacial protonation reaction

To better understand the interfacial state and manipulate the interfacial protonation reaction, an external mechanical force<sup>47–49</sup> is further used to control the single-event protonation reaction at the metal-solution interface. External mechanical forces are typically employed to manipulate the conductance switching in single-molecule junctions. During these single-molecule electrical measurements, the upper tip was continuously pulled away from the substrate at a rate of  $18.6 \text{ nm s}^{-1}$ , exerting an external mechanical force on the SMJ. 1D and 2D single-molecule conductance-displacement histograms for TP-N molecular junctions at TFMS concentrations of 0.83 to 5.83 mM are shown in Fig. 5a and Supplementary Fig. 17. Similar to the behavior when hovering without an external mechanical force, an obvious conductance peak from State 2 can be observed when the acid concentration reaches 0.83 mM (Fig. 5a). As the TFMS concentration escalates from 0.83 to 5.83 mM, the proportion of State 1 declines, while the proportion of State 2 rises accordingly. (Supplementary Fig. 15b). Similar to  $A_{S2}/A_{S1}$  value without force, as the acid concentration increases,  $A_{S2}/A_{S1}$  value under force also changes slowly at first and then sharply from 0.59 to 11.37 (Fig. 5b). More detailed, when the acid concentration is below 3.33 mM,  $A_{S2}/A_{S1}$  value with force is larger than that without force, meaning that the applied external mechanical force promotes the formation of the protonated state. One reasonable explanation is that when the tip is kept pulling up, the N–Au dative bond may be attenuated and the proton may have a higher possibility to insert between the amino group and the gold atom, thus promoting the interfacial protonation reaction (Fig. 5c). When the acid concentration exceeds 3.33 mM,  $A_{S2}/A_{S1}$  value under force is relatively small. At an acid concentration of 3.33 mM acid,  $\tau_{S2}$  in hover mode exceeds 33.7 ms (Fig. 4b). However, the conductance plateau length under the force is only 0.59 nm (without considering the snap-back distance) (Supplementary Fig. 18), indicating that the SMJ exists for

31.7 ms. Therefore, under an external mechanical force, the SMJ breaks before State 2 reaches its lifetime. Because the external mechanical force affects the stability of State 2,  $A_{S2}/A_{S1}$  value under force at high acid concentration is smaller than that without force (Fig. 5c). In addition, the conductance plateau length of State 2 diminishes with an increase in acid concentration (Supplementary Fig. 18h), indicating that protons influence the stability of State 2. The conductance plateau length of the initial state is shown in Supplementary Fig. 19.

In conclusion, this work in-situ investigates the protonation reaction dynamics of amino groups at the metal-solution interface from the single-event perspective. A stable cationic interfacial state has been discovered, which provides the basis for detecting interfacial protonation reactions. Through real-time single-molecule electrical measurements, in-situ monitoring of protonation reactions at the single-event level has been achieved. By further analyzing the dynamics of protonation reactions, the reaction process has been revealed. Then, the effect of acid concentration on reversible single-event protonation reaction has also been studied. The rate constant of protonation is positively linearly correlated with acid concentration, whereas that of deprotonation is negatively linearly correlated. In addition, when an external mechanical force is exerted on the SMJ, the force can effectively regulate the interfacial protonation reaction by promoting the forward reaction process. The study of solid-liquid interfacial protonation reaction dynamics at the single-event level provides a possibility for promoting the development of interface science, which will be beneficial for the fields of heterogeneous catalysis and electrochemistry.

## Methods

### Experimental preparation

The gold tip (diameter = 0.25 mm, 99.99% purity, ZhongNuo Advanced Material (Beijing) Technology Co., Ltd) was obtained by

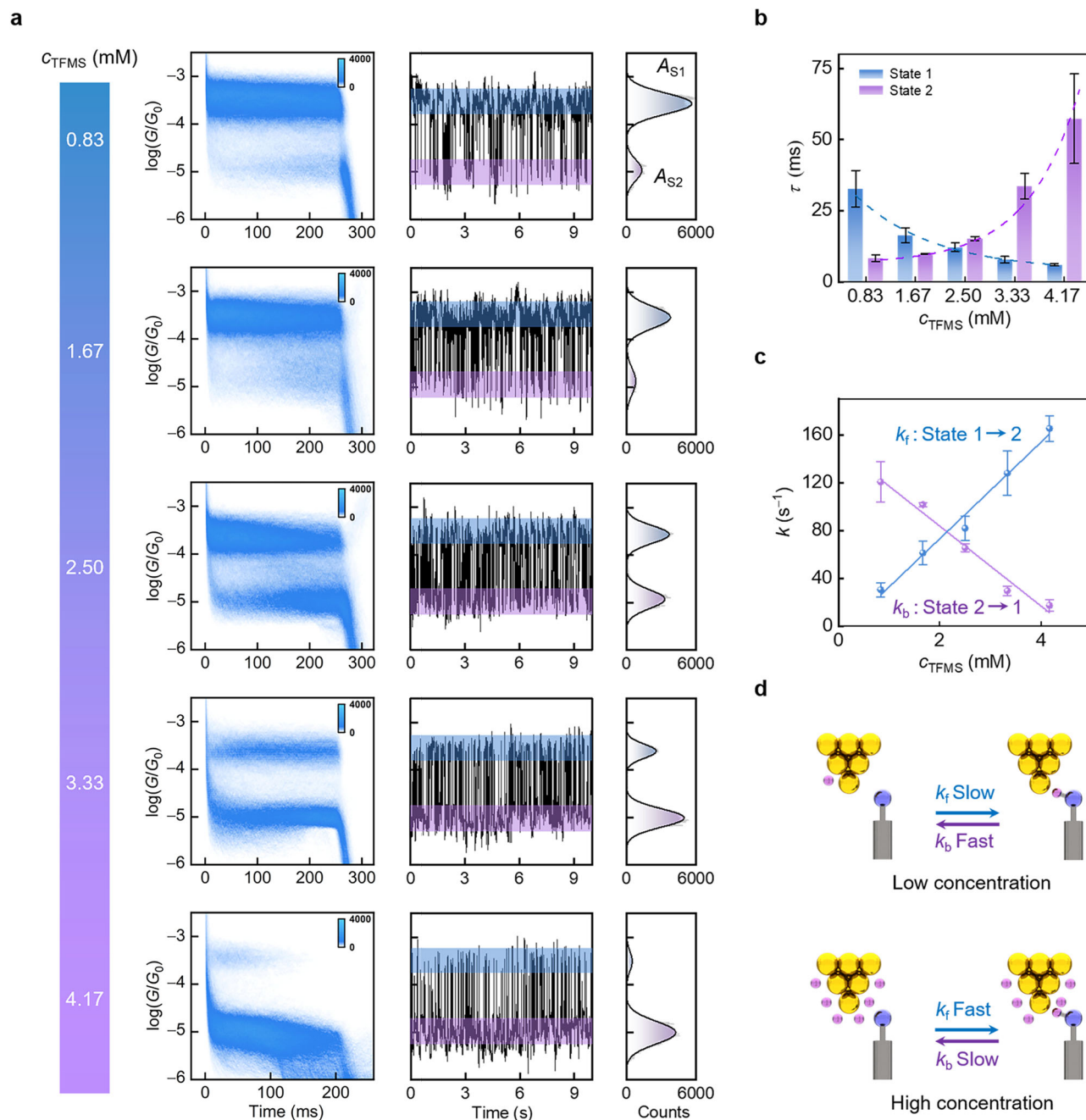


**Fig. 4 | Proton concentration-dependent measurements.** **a**  $G$ - $t$  traces and corresponding histograms of single-molecule junctions measured in the reaction solutions with different acid concentrations. The color scale shows the counts. **b,c** Changes in lifetime (**b**) and rate constant (**c**) of State 1 (blue) and State 2 (purple) at different acid concentrations. The error scales were derived from the

corresponding single exponential fittings of the dwell times (standard deviation) and the number of independent samples is  $\approx 200$ . **d** Schematic diagram for the effect of acid concentrations on the protonation reaction at the metal-solution interface. Au, C, N, and H atoms are depicted in yellow, gray, blue, and purple, respectively. Source data are provided as a Source Data file.

electrochemical corrosion and was coated with Apiezon wax to suppress the background conductance of the solution. The gold substrate was prepared by evaporating 8-nm-thick chromium at  $0.05 \text{ \AA s}^{-1}$  and 100-nm-thick gold at  $0.15 \text{ \AA s}^{-1}$  on a clean silicon wafer. TP-N (Mreda, 98% purity), TP-S, BP-S (Bide, 98% purity), TFMS (Macklin, 98% purity), and TFA (Macklin, 99.9% purity) were dissolved in PC (Macklin, 99% purity), respectively. All reagents were used without further purification.

Before STM-BJ measurement, different ratios of molecular solution and acid solution were mixed and stirred. During the STM-BJ experiment,  $2 \mu\text{L}$  mixed solution was added to the Au substrate. The bias voltage applied to the molecular junction was  $0.1\text{V}$ . The time

resolution of the measurement was  $20 \text{ kHz}$  ( $50 \mu\text{s}$ ). All measurements were carried out at room temperature by X-tech STM-BJ purchased from VR (Xiamen) Technology Company, China, and the data was analyzed by XMe open-source code ([https://github.com/Pilab-XMU/XMe\\_DataAnalysis](https://github.com/Pilab-XMU/XMe_DataAnalysis))<sup>50</sup>. There are two kinds of working modes in STM-BJs. One is the conductance-displacement measurement, where the tip is retracted from the substrate continuously and an external mechanical force is exerted on the single-molecule system. The other one is the conductance-time measurement (hover mode), where the tip is halted for  $200 \text{ ms}$  after single-molecule junction formation and no external mechanical force is exerted. Both 1D and 2D conductance-displacement or conductance-time histograms are analyzed without

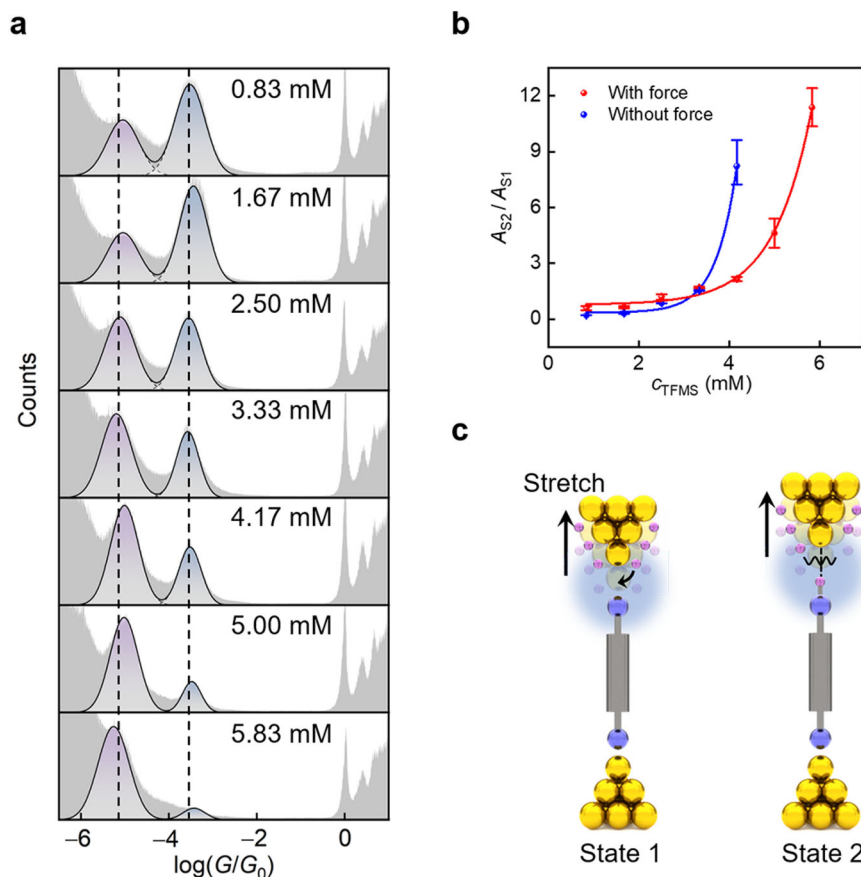


**Fig. 5 | Reaction manipulation under an external mechanical force.** **a** 1D conductance histograms for TP-N molecular junctions with different acid concentrations under forces. **b** Changes in area ratios of State 2 over State 1 with (red) or without (blue) forces. The error scales were derived from the thousands of single-

molecule experiments (standard deviation). **c** Schematic diagram for the force manipulation of single-molecule junctions in State 1 and State 2. Au, C, N, and H atoms are depicted in yellow, gray, blue, and purple, respectively. Source data are provided as a Source Data file.

any data selection. Gaussian fitting is applied to fit the conductance peaks and the integrated areas under the fitted curves are considered as the peaks' areas.

### Molecular synthesis of TP-S

All reagents and solvents used in the synthesis procedure of 4'-amino-4-thiol-*p*-terphenyl (TP-S) were commercially available and used without further purification (99.7% purity). Thin layer chromatography (TLC) silica gel plate was used to monitor the reaction. Flash column chromatography was made from silica gel from Shenghai Qingdao (300–400 mesh).  $^1\text{H}$  and  $^{13}\text{C}$  NMR spectra were recorded in  $\text{CDCl}_3$  on a Bruker Avance 400 MHz spectrometer. High-resolution mass spectrometric analysis was conducted within the ESI mode on Thermo Q Exactive Focus.

Chemical structures and the detailed synthetic pathway of TP-S molecule are shown in Supplementary Fig. 1. The synthesis of TP-S was successfully prepared in a yield of 35.0% by reducing the corresponding nitroarenes 4'-nitro-[1,1':4',1''-terphenyl]-4-thiol (TPT-NO<sub>2</sub>). TPT-NO<sub>2</sub> was synthesized according to ref. 51. Compound **2** was obtained via Suzuki coupling of **1** with (4-nitrophenyl)boronic acid, which was commercially available. After that, an intermolecular nucleophilic substitution reaction of **2** with dimethylcarbamoyl chloride using sodium hydride as base to obtain compound **3**, which was heated to 210 °C without any solvent for 18 h to afford the key intermediate **4** via a Newman-Kwart rearrangement. Finally, hydrolysis reaction of **4** by potassium hydroxide in methanol was carried out to give TPT-NO<sub>2</sub>.

Under N<sub>2</sub> atmosphere, the mixture of TPT-NO<sub>2</sub><sup>51</sup> (0.15 g, 0.47 mmol, 1.0 eq), SnCl<sub>2</sub>·2H<sub>2</sub>O (1.09 g, 2.35 mmol, 5.0 eq), HCl (0.3 mL) in 15 mL of ethanol was heated to 80 °C in a two necked bottle for 8 h. Upon cooling to room temperature, the resulting solution was poured into 30 mL of ice-cold water and slowly added 2 M aqueous NaOH until the pH reached 9. The aqueous solution was then extracted with DCM (3×10 mL) three times. After drying with anhydrous Na<sub>2</sub>SO<sub>4</sub>, the organic layers were concentrated in reduced pressure. The crude product was purified by flash column chromatography to obtain the product as a yellow solid (0.047 g, 35%). The product has low solubility in  $\text{CDCl}_3$  and other solvents. TLC (PE:CH<sub>2</sub>Cl<sub>2</sub>, 1:3, v/v):  $R_f$  = 0.5;  $^1\text{H}$  NMR (400 MHz,  $\text{CDCl}_3$ ): (ppm) 7.76 (s, 4H), 7.51 (d,  $J$  = 8.0 Hz, 2H), 7.46 (d,  $J$  = 8.0 Hz, 2H), 7.35 (d,  $J$  = 8.0 Hz, 2H), 6.77 (d,  $J$  = 8.0 Hz, 2H), 3.76 (brs, 2H), 3.49 (s, 1H); ESI HRMS  $m/z$ :  $[\text{M} + \text{H}]^+$  calcd for C<sub>18</sub>H<sub>16</sub>NS 278.0998, found 278.0999. In the  $^1\text{H}$  NMR spectrum of TP-S, the singlet peak at ≈3.49 ppm can be assigned to the proton in the sulfur atom. The broad peak at ≈3.76 ppm is attributed to the characteristic peak of amino compounds which is consistent with refs. 28,52.

### Computational methods

The geometric and electronic properties of the molecular junction were calculated using density functional theory (DFT). The PBE functional<sup>53</sup> was used for the correlation-exchange interactions, and the dispersion interactions were included by using the DFT-D3 method<sup>54</sup>. A proton was added to model the proton environment, and a fluorine anion was used to balance the positive charge. The solvation effects were considered by using an implicit solvent model<sup>55,56</sup>. The transition states were located

using the climbing-image nudged elastic band (CI-NEB) method<sup>57</sup> and vibrational analysis was performed to verify the transition states. The calculations of transmission spectra were performed by combining DFT with the nonequilibrium Green's function (NEGF) method<sup>58</sup>. Since the fluorine atom employed for the charge balance introduces artificial energy levels that interfere with calculated transmission spectra, we adopted a different charge balance scheme as in ref. 59, to account for the charge and counter ion, i.e., atomic compensation charge was applied to take out an electron from the associated hydrogen atom and background electron charge was added to neutralize the system. Details of the computational methods and the simulation model are provided in Supplementary Note 3.

## Data availability

The data that support the findings of this study are available from Zenodo<sup>60</sup> and from the corresponding authors upon request. Source data are provided with this paper.

## References

- Chen, G. F. et al. Electrochemical reduction of nitrate to ammonia via direct eight-electron transfer using a copper-molecular solid catalyst. *Nat. Energy* **5**, 605–613 (2020).
- Dai, J. et al. Hydrogen spillover in complex oxide multifunctional sites improves acidic hydrogen evolution electrocatalysis. *Nat. Commun.* **13**, 1189 (2022).
- Ro, I. et al. Bifunctional hydroformylation on heterogeneous Rh-WO<sub>x</sub> pair site catalysts. *Nature* **609**, 287–292 (2022).
- Favaro, M. et al. Unravelling the electrochemical double layer by direct probing of the solid/liquid interface. *Nat. Commun.* **7**, 12695 (2016).
- Ryu, J. et al. Thermochemical aerobic oxidation catalysis in water can be analysed as two coupled electrochemical half-reactions. *Nat. Catal.* **4**, 742–752 (2021).
- Yu, Y. et al. Tunable angle-dependent electrochemistry at twisted bilayer graphene with moire flat bands. *Nat. Chem.* **14**, 267–273 (2022).
- Geng, J. et al. Ambient electrosynthesis of urea with nitrate and carbon dioxide over iron-based dual-sites. *Angew. Chem. Int. Ed.* **62**, e202210958 (2023).
- Li, M. et al. Electrosynthesis of amino acids from NO and  $\alpha$ -keto acids using two decoupled flow reactors. *Nat. Catal.* **6**, 906–915 (2023).
- Stamenkovic, V. R. et al. Energy and fuels from electrochemical interfaces. *Nat. Mater.* **16**, 57–69 (2016).
- Wang, Y. H. et al. In situ Raman spectroscopy reveals the structure and dissociation of interfacial water. *Nature* **600**, 81–85 (2021).
- Wang, T. et al. Enhancing oxygen reduction electrocatalysis by tuning interfacial hydrogen bonds. *Nat. Catal.* **4**, 753–762 (2021).
- Li, P. et al. Single-molecule optoelectronic devices: physical mechanism and beyond. *Opto-Electron. Adv.* **5**, 210094 (2022).
- Li, P. et al. Single-molecule nano-optoelectronics: insights from physics. *Rep. Prog. Phys.* **85**, 086401 (2022).
- Yang, C. et al. Graphene-molecule-graphene single-molecule junctions to detect electronic reactions at the molecular scale. *Nat. Protoc.* **18**, 1958–1978 (2023).
- Xu, B. et al. Measurement of single-molecule resistance by repeated formation of molecular junctions. *Science* **301**, 1221–1223 (2003).
- Chen, H. et al. Reactions in single-molecule junctions. *Nat. Rev. Mater.* **8**, 165–185 (2022).
- Guo, X. et al. Covalently bridging gaps in single-walled carbon nanotubes with conducting molecules. *Science* **311**, 356–359 (2006).
- Audi, H. et al. Electrical molecular switch addressed by chemical stimuli. *Nanoscale* **12**, 10127–10139 (2020).
- Morales, G. M. et al. Inversion of the rectifying effect in diblock molecular diodes by protonation. *J. Am. Chem. Soc.* **127**, 10456–10457 (2005).
- Darwish, N. et al. Multi-responsive photo- and chemo-electrical single-molecule switches. *Nano Lett* **14**, 7064–7070 (2014).
- Yang, C. et al. Electric field-catalyzed single-molecule Diels-Alder reaction dynamics. *Sci. Adv.* **7**, eabf0689 (2021).
- Yang, C. et al. Unveiling the full reaction path of the Suzuki-Miyaura cross-coupling in a single-molecule junction. *Nat. Nanotechnol.* **16**, 1214–1223 (2021).
- Zhang, L. et al. Precise electrical gating of the single-molecule Mizoroki-Heck reaction. *Nat. Commun.* **13**, 4552 (2022).
- Yang, C. et al. Real-time monitoring of reaction stereochemistry through single-molecule observations of chirality-induced spin selectivity. *Nat. Chem.* **15**, 972–979 (2023).
- Cao, Y. et al. Building high-throughput molecular junctions using indented graphene point contacts. *Angew. Chem. Int. Ed.* **51**, 12228–12232 (2012).
- Li, C. et al. Charge transport in single Au|alkanedithiol|Au junctions: coordination geometries and conformational degrees of freedom. *J. Am. Chem. Soc.* **130**, 318–326 (2008).
- Huang, X. et al. Electric field-induced selective catalysis of single-molecule reaction. *Sci. Adv.* **5**, eaaw3072 (2019).
- Zang, Y. et al. In situ coupling of single molecules driven by gold-catalyzed electrooxidation. *Angew. Chem. Int. Ed.* **58**, 16008–16012 (2019).
- Chen, H. et al. Single-molecule charge transport through positively charged electrostatic anchors. *J. Am. Chem. Soc.* **143**, 2886–2895 (2021).
- Chen, H. et al. Electron-catalyzed dehydrogenation in a single-molecule junction. *J. Am. Chem. Soc.* **143**, 8476–8487 (2021).
- Zhang, A. et al. Catalytic cycle of formate dehydrogenase captured by single-molecule conductance. *Nat. Catal.* **6**, 266–275 (2023).
- Ballesteros, L. M. et al. Controlling the structural and electrical properties of diacid oligo(phenylene ethynylene) Langmuir-Blodgett films. *Chem. Eur. J.* **19**, 5352–5363 (2013).
- Brooke, R. J. et al. Dual control of molecular conductance through pH and potential in single-molecule devices. *Nano Lett* **18**, 1317–1322 (2018).
- Tian, Y. et al. Visualizing Eigen/Zundel cations and their interconversion in monolayer water on metal surfaces. *Science* **377**, 315–319 (2022).
- Kosmala, T. et al. Operando visualization of the hydrogen evolution reaction with atomic-scale precision at different metal-graphene interfaces. *Nat. Catal.* **4**, 850–859 (2021).
- Yanson, A. I. et al. Formation and manipulation of a metallic wire of single gold atoms. *Nature* **395**, 783–785 (1998).
- Venkataraman, L. et al. Dependence of single-molecule junction conductance on molecular conformation. *Nature* **442**, 904–907 (2006).
- Tang, Y. et al. Electric field-induced assembly in single-stacking terphenyl junctions. *J. Am. Chem. Soc.* **142**, 19101–19109 (2020).
- Zang, Y. et al. Electronically transparent Au-N bonds for molecular junctions. *J. Am. Chem. Soc.* **139**, 14845–14848 (2017).
- Chen, F. et al. Effect of anchoring groups on single-molecule conductance: comparative study of thiol-, amine-, and carboxylic-acid-terminated molecules. *J. Am. Chem. Soc.* **128**, 15874–15881 (2006).
- Becke, A. D. et al. A simple measure of electron localization in atomic and molecular systems. *J. Chem. Phys.* **92**, 5397–5403 (1990).
- Milescu, L. S. et al. Maximum likelihood estimation of molecular motor kinetics from staircase dwell-time sequences. *Biophys. J.* **91**, 1156–1168 (2006).
- Guan, J. et al. Direct single-molecule dynamic detection of chemical reactions. *Sci. Adv.* **4**, eaar2177 (2018).

44. Castro, C. et al. Heavy-atom tunneling in organic reactions. *Angew. Chem. Int. Ed.* **59**, 8355–8366 (2020).
45. Schleif, T. et al. Solvation effects on quantum tunneling reactions. *Acc. Chem. Res.* **55**, 2180–2190 (2022).
46. Wild, R. et al. Tunnelling measured in a very slow ion–molecule reaction. *Nature* **615**, 425–429 (2023).
47. Quek, S. Y. et al. Mechanically controlled binary conductance switching of a single-molecule junction. *Nat. Nanotechnol.* **4**, 230–234 (2009).
48. Li, J. et al. Mechanical single-molecule potentiometers with large switching factors from *ortho*-pentaphenylene foldamers. *Nat. Commun.* **12**, 167 (2021).
49. Zhou, P. et al. Robust single-supermolecule switches operating in response to two different noncovalent interactions. *J. Am. Chem. Soc.* **145**, 18800–18811 (2023).
50. Pan, Z. et al. XMe-Xiamen molecular electronics code: An intelligent and open-source data analysis tool for single-molecule conductance measurements. *Chin. J. Chem.* **42**, 317–329 (2023).
51. Waske, P. et al. Nitro-substituted aromatic thiolate self-assembled monolayers: structural properties and electron transfer upon resonant excitation of the tail group. *J. Phys. Chem. C* **118**, 26049–26060 (2014).
52. Mou, J. et al. Structure-activity relationship study of E6 as a novel necroptosis inducer. *Bioorganic. Med. Chem. Lett.* **25**, 3057–3061 (2015).
53. Perdew, J. P. et al. Generalized gradient approximation made simple. *Phys. Rev. Lett.* **77**, 3865–3868 (1996).
54. Grimme, S. et al. A consistent and accurate ab initio parametrization of density functional dispersion correction (DFT-D) for the 94 elements H–Pu. *J. Chem. Phys.* **132**, 154104 (2010).
55. Mathew, K. et al. Implicit solvation model for density-functional study of nanocrystal surfaces and reaction pathways. *J. Chem. Phys.* **140**, 084106 (2014).
56. Mathew, K. et al. Implicit self-consistent electrolyte model in plane-wave density-functional theory. *J. Chem. Phys.* **151**, 234101 (2019).
57. Henkelman, G. et al. A climbing image nudged elastic band method for finding saddle points and minimum energy paths. *J. Chem. Phys.* **113**, 9901–9904 (2000).
58. Brandbyge, M. et al. Density-functional method for nonequilibrium electron transport. *Phys. Rev. B* **65**, 165401 (2002).
59. Lei, S. et al. Surface functionalization of two-dimensional metal chalcogenides by Lewis acid–base chemistry. *Nat. Nanotechnol.* **11**, 465–471 (2016).
60. Zhao, C. Electrical monitoring of single-event protonation dynamics at the solid–liquid interface and its regulation by external mechanical forces. *Zenodo*, <https://doi.org/10.5281/zenodo.13644448> (2024).

## Acknowledgements

The authors acknowledge primary financial support from the National Key R&D Program of China (2021YFA1200101 (to X.G.), 2022YFE0128700 (to X.G.), and 2021YFA1200102 (to C.J.)), the National Natural Science Foundation of China (22150013 (to X.G.), 21727806 (to X.G.), 21933001 (to X.G.), 22173050 (to C.J.), 22273091 (to Q.F.), and 22205117 (to G.L.)),

the Natural Science Foundation of Beijing (2222009 (to X.G.)), Beijing National Laboratory for Molecular Sciences (BNLMS-CXXM-202407 (to X.G.)), the Chinese Academy of Sciences (CAS) Project for Young Scientists in Basic Research (YSBR-054 (to Q.F.)), and the Innovation Program for Quantum Science and Technology (2021ZD0303302 (to Q.F.)). Q.F. thanks the USTC supercomputing center for providing computational resources for this project.

## Author contributions

X.G. and C.J. conceived the idea for the paper. C.Z. carried out the experimental measurements. J.D. and J.H. built and analyzed the theoretical model and performed the quantum transport calculation. G.L. and Z.L. carried out the molecular synthesis. X.G., C.J., Q.F., X.L., G.L., C.Z., J.D., Z.L., J.H., S.H., and S.L. analyzed the data and wrote the paper. All the authors discussed the results and commented on the manuscript.

## Competing interests

The authors declare no competing interests.

## Additional information

**Supplementary information** The online version contains supplementary material available at <https://doi.org/10.1038/s41467-024-53179-4>.

**Correspondence** and requests for materials should be addressed to Guangwu Li, Qiang Fu, Chuancheng Jia or Xuefeng Guo.

**Peer review information** *Nature Communications* thanks the anonymous reviewers for their contribution to the peer review of this work. A peer review file is available.

**Reprints and permissions information** is available at <http://www.nature.com/reprints>

**Publisher's note** Springer Nature remains neutral with regard to jurisdictional claims in published maps and institutional affiliations.

**Open Access** This article is licensed under a Creative Commons Attribution-NonCommercial-NoDerivatives 4.0 International License, which permits any non-commercial use, sharing, distribution and reproduction in any medium or format, as long as you give appropriate credit to the original author(s) and the source, provide a link to the Creative Commons licence, and indicate if you modified the licensed material. You do not have permission under this licence to share adapted material derived from this article or parts of it. The images or other third party material in this article are included in the article's Creative Commons licence, unless indicated otherwise in a credit line to the material. If material is not included in the article's Creative Commons licence and your intended use is not permitted by statutory regulation or exceeds the permitted use, you will need to obtain permission directly from the copyright holder. To view a copy of this licence, visit <http://creativecommons.org/licenses/by-nc-nd/4.0/>.

© The Author(s) 2024